

# Structure and stability of Sb/Au(110)-c(2 × 2) surface phase

P.F. Lyman\*, V.L. Shneerson, R. Fung, S.S. Parihar, H.T. Johnson-Steigelman,  
E.D. Lu, D.K. Saldin

*Department of Physics and the Laboratory for Surface Studies, University of Wisconsin-Milwaukee, Physics Building, 1900 E. Kenwood Blvd., Milwaukee, WI 53211, USA*

Received 14 April 2005; accepted for publication 2 November 2005  
Available online 19 December 2005

## Abstract

Adsorption of 0.5 monolayers (ML) of Sb on the Au(110) surface resulted in the formation of a c(2 × 2) surface reconstruction. Analysis of surface X-ray diffraction data by a direct method revealed the existence of an ordered substitutional surface alloy, with every other hollow site occupied by Au and Sb atoms. Quantitative conventional  $\chi^2$  refinement showed a contraction of  $0.12 \pm 0.03$  Å in the spacing of the first Au layer to the second, an expansion of  $0.13 \pm 0.03$  Å in the second-to-third layer distance, and an inward Sb displacement (rumpling) of  $0.21 \pm 0.04$  Å. This surface phase proved to be extremely robust, with the long-range order of this arrangement remaining up to substrate temperatures of 900 K.

© 2005 Elsevier B.V. All rights reserved.

*Keywords:* Direct methods in crystallography; X-ray scattering, diffraction and reflection; Low-energy electron diffraction (LEED); Surface relaxation and reconstruction; Phase transition; Surface segregation; Gold; Antimony

## 1. Introduction

Sb and Au are historically linked by their frequent joint appearance in auriferous ores: along with As, Sb is one of the major “pathfinders” for commercial Au deposits [1]. In early semiconductor devices, the Au:Sb system was of interest for forming contacts to n-type materials: the Sb segregates to the interface and aids in the formation of an Ohmic junction with the semiconductor [2]. Recently, interest in this system has arisen due to a potential role in Pb-free solders for microelectronics [3] and for the size-dependent crystallization properties [4], spontaneous room-temperature [4,5] and low-temperature [6] alloy formation and solubility anomalies [4] exhibited in the nano-scale regime.

These surface and interface properties are intimately related to the bulk Sb:Au phase diagram: they form a strongly bound compound (AuSb<sub>2</sub>) [7], and the solid solu-

bility of Sb in fcc Au is limited to less than 1.2% [8,9]. These conditions favor a strong segregation of any bulk Sb to the Au surface [10,11]. Indeed, it has been demonstrated previously that the Sb surface-to-bulk concentration ratio in Au can exceed  $10^4$  [12]. Thus, the segregation-induced “confinement” of Sb to the surface selvage region, coupled with the chemical affinity of the two metals, may result in the formation of surface alloys and/or compounds unknown in the bulk. Here, we report the formation of a Sb/Au(110)-c(2 × 2) phase. To our knowledge, the Sb/Au(110) surface/adsorbate system has not been previously reported on in the literature.

We have employed surface X-ray diffraction (SXR) to uncover the structure of this phase. Often, the most difficult step in determining a structure using SXR is not refining the fit parameters of a model, but generating a starting structure to refine [13]. Notably, we have used a new analytical technique [14–17] to visualize the atomic geometry of the near-surface region. This direct method allows one to generate, independent of any preconceived model, a robust image of the atomic arrangements at the surface. This image

\* Corresponding author. Tel.: +1 414 229 4626; fax: +1 414 229 5589.  
E-mail address: [plyman@uwm.edu](mailto:plyman@uwm.edu) (P.F. Lyman).

guides further refinement of the atomic locations by conventional  $\chi^2$  fitting. In absence of such a visualization, the investigator must imagine, through chemical intuition or other means, a correct starting model to refine. While this has often been possible, as witnessed by the success of SXRD studies over the last 25 years, incorrect starting models are extremely unlikely to refine to the correct one. If the number or identity of the atoms in the proposed model is incorrect, then such convergence becomes impossible.

We have previously demonstrated the feasibility of this direct-method algorithm by applying it to a surface reconstruction whose structure was already known [17]. In the present work, we use it on a system that was previously unreported in the literature, so no proposed models were available. As will be discussed, this analytical method was able to guide us to the correct structure, where conventional means would have met pitfalls.

## 2. Theory of the direct method

In X-ray diffraction from a crystal surface, the breaking of the crystal periodicity perpendicular to the surface broadens the Bragg spots into streaks perpendicular to the surface in reciprocal space, referred to as *crystal truncation rods* (CTRs) [18,19]. If the surface is reconstructed, the diffraction conditions give rise to extra reciprocal-lattice rods known as *superstructure rods* (SRs). A SXRD experiment may measure the intensities along each of these types of rods as functions of reciprocal-space coordinates  $\vec{q}$ . The aim of surface crystallography is the determination of the atomic structure of the surface layers insofar as they differ from the known bulk. Our direct method for SXRD [14–17] takes as input only measured intensities of CTRs and SRs and a knowledge of the bulk structure, and gives as output the 3D electron density of an entire surface unit cell (to a depth where the structure is indistinguishable from that of the bulk).

Our scheme employs an iterative algorithm that alternately satisfies constraints in real and reciprocal space [20], and is illustrated in Fig. 1. A full description of the algorithm, including procedures necessary for application

to experimental data, will be published elsewhere [21]. Briefly, a trial solution of a set of structure factors  $\{F(\vec{q})\}$  is chosen, having magnitudes equal to those measured in the experiment, but with random phases. After subtracting off the calculable bulk contribution  $\{B(\vec{q})\}$ , the remaining contribution provides an estimate of the surface scattering factor  $\{S(\vec{q})\}$ . These are Fourier transformed to give an estimate  $\{u(\vec{x})\}$  of the electron density distribution in real space. In general, this estimate will extend unphysically far from the surface region, so any recovered density beyond a certain distance from the surface is simply set equal to zero. Next, the remaining density  $\{u(\vec{x})\}$  is transformed back into reciprocal space to render an improved estimate of the surface scattering factor  $\{S(\vec{q})\}$ , and the calculable bulk contribution  $\{B(\vec{q})\}$  is added back to this. The phases of this sum are then assigned to the measured magnitudes, yielding an improved estimate of  $\{F(\vec{q})\}$ . This cycle is repeated until the density  $\{u(\vec{x})\}$  does not appreciably change during a cycle. We find that this process converges to a solution that corresponds in reciprocal space to the measured structure factor amplitudes, and that is confined in real space to the near-surface region. Peaks in this distribution would be expected to reveal the positions of atoms in the surface unit cell.

## 3. Experimental details

Experiments were carried out in two separate ultrahigh vacuum (UHV) chambers. Initial experiments were carried out at the University of Wisconsin-Milwaukee in a chamber equipped with low-energy electron diffraction (LEED) and X-ray photoelectron spectroscopy (XPS) capabilities. Quantitative structural measurements were made using SXRD at beamline X22C at the National Synchrotron Light Source (NSLS) at Brookhaven National Laboratory. The X22C endstation [22] is equipped with a 6-circle diffractometer for SXRD measurements, and a UHV chamber with a cylindrical mirror analyzer for Auger electron spectroscopy. During the SXRD measurements, the surface temperature was monitored using a W-WRe thermocouple attached directly to the sample, while temperatures in the XPS chamber were evaluated using a low-temperature infrared pyrometer.

The mechanically polished Au(110) single crystal was annealed in vacuum at 1175 K for 15 h to reduce the bulk mosaic spread to  $<0.04^\circ$ , and subsequently electropolished to remove the damaged and roughened surface layers. The surface was first prepared to be atomically clean by standard  $\text{Ar}^+$  sputtering and annealing cycles, and exhibited the well-known  $(2 \times 1)$  reconstruction [23]. Monolayer (ML,  $1 \text{ ML} = 8.50 \times 10^{14} \text{ cm}^{-2}$ ) quantities of Sb (99.9999% purity) were then deposited on the substrate from an effusion cell operated at 680 K. Both deposition onto a RT substrate with post-annealing to 700 K and deposition onto a substrate held at either 540 K or 700 K were investigated. In either case, the samples were typically held at 700 K for 5 min after deposition ceased, and then slowly

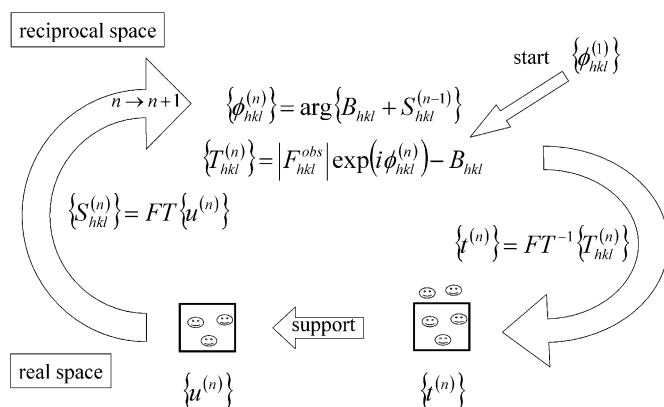


Fig. 1. Schematic flowchart of iterative phase recovery algorithm.

cooled. This annealing temperature is near the  $(2 \times 1) \rightarrow (1 \times 1)$  deconstruction temperature (735 K) [24,25] and above the Sb:Au eutectic temperature (630 K) [7–9], but below the temperature at which the clean surface roughens ( $\sim 784$  K) [24]. Thus, the surface system had sufficient mobility and thermal activation to reach its quasi-equilibrium RT state upon slow cooling.

XP spectra were obtained from the resultant Sb/Au(110) surfaces using unmonochromated Al  $K_{\alpha}$  radiation and a hemispherical analyzer operated at 50 eV pass energy, yielding a total energy resolution of 1.0 eV. The Au  $4p_{3/2}$ , Sb  $3d_{3/2}$ , and Sb  $3d_{5/2}$  core levels were recorded in a single spectrum with well-resolved features. Wide energy scans showed no other impurity species. The spectra were numerically fit using a combination of an inelastic background function [26] and asymmetric (Doniach–Sunjic) lineshapes [27]. The XP spectra were used to determine the Sb coverage and to correlate it with the LEED pattern observed.

Radiation of 10.8 keV was used to acquire the SXRD data. Following convention, the coordinate system has two vectors in the surface plane, with the third arranged perpendicular to the surface. Thus, the real-space unit cell was chosen to be  $\mathbf{a}_1 = \frac{1}{2}[\bar{1}10]_{\text{cub}}$ ,  $\mathbf{a}_2 = [001]_{\text{cub}}$ , and  $\mathbf{a}_3 = \frac{1}{2}[110]_{\text{cub}}$ , where the subscript refers to the conventional fcc cell, and the reciprocal-space coordinate system is then  $\mathbf{b}_1 = (\bar{1}10)_{\text{cub}}$ ,  $\mathbf{b}_2 = (001)_{\text{cub}}$ , and  $\mathbf{b}_3 = (110)_{\text{cub}}$ . In this frame, the index  $l$  refers to momentum transfer  $q_{\perp}$  perpendicular to the surface plane, while the indices  $h$  and  $k$  refer to in-plane momentum transfer  $q_{\parallel}$ . The angle of incidence was kept equal to the exit angle to allow access to large values ( $\approx 4 \text{ \AA}^{-1}$ ) of  $q_{\perp}$ , while still accessing up to  $q_{\parallel} \approx 10 \text{ \AA}^{-1}$ . The measured structure factors were corrected [28] for geometrical and polarization effects. Approximately 1200 surface structure factor amplitudes were measured, covering 558 non-equivalent reflections distributed along 41  $(hk)$  rods. In terms of the Laue indices, this encompassed the range  $0 \leq h \leq 4$ ,  $0 \leq k \leq 4$ , and  $0 \leq l \leq 1.8$ . Both crystal truncation rods (CTR) [18,19], which arise from the termination of the bulk, and superstructure rods (SR), which arise from a change in the lateral length scale due to surface reconstruction, were recorded over this range.

#### 4. XPS and LEED results

Upon Sb deposition and annealing, several different surface reconstructions were observed in LEED, depending on Sb coverage. None of these have been reported in the literature before. The pattern corresponding to the lowest Sb coverage has  $c(2 \times 2)$  symmetry, as shown in Fig. 2. (We also observed  $(\sqrt{3} \times \sqrt{3})R54.7^{\circ}$  and  $p(5 \times 6)$  patterns, and are currently investigating the structure of those reconstructions.) LEED patterns were clear and sharp from quite low energies to hundreds of eV; in contrast, the surface structure found on Sb/Au(100) displayed a clear LEED pattern only at low incident energies [12].

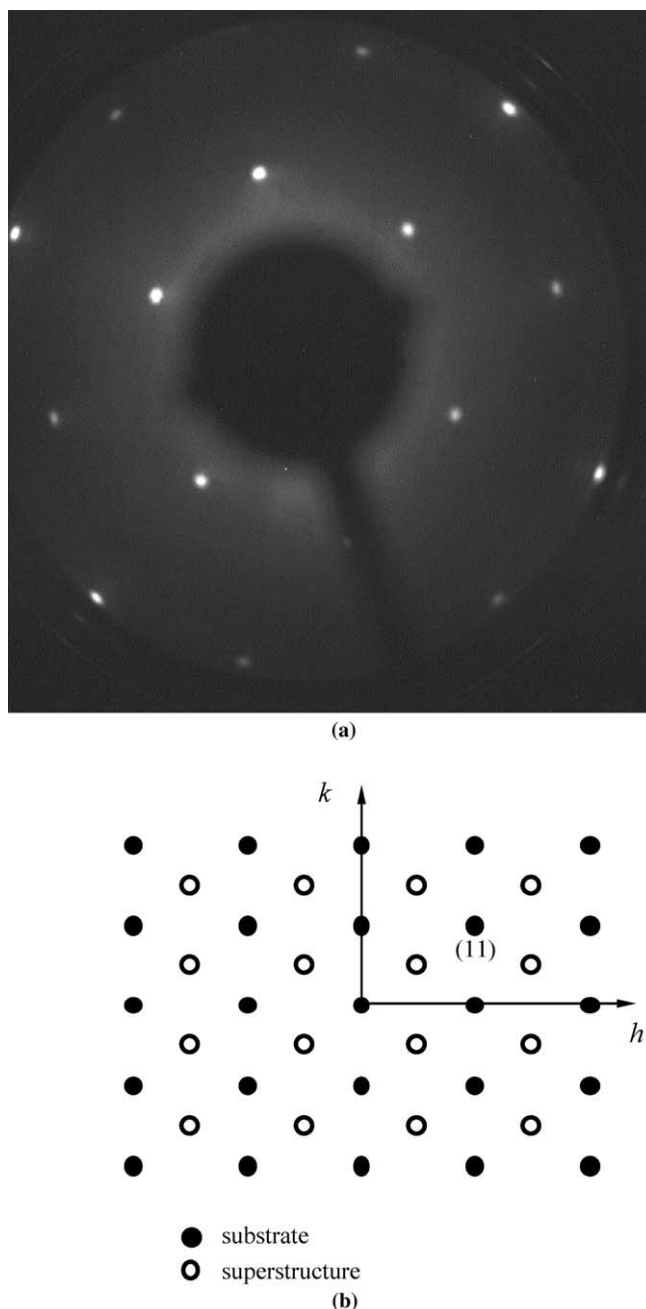


Fig. 2. (a) Low-energy electron diffraction (LEED) pattern of a 0.5 ML Sb/Au(110)- $c(2 \times 2)$  surface acquired at 44 eV. (b) Schematic diagram of this pattern.

We prepared each surface phase by depositing enough Sb to form one of the ordered reconstructions while the substrate was held either at room-temperature (RT), 540 K, or 700 K. In all cases, deposition was followed by annealing to 700 K. No differences were observed in the LEED pattern depending on initial deposition temperature. After investigating such a phase, we sputtered the surface clean while the sample was held at RT, and re-annealed; instead of obtaining the expected clean-surface Au(110)- $(2 \times 1)$  reconstruction, we observed the Sb/

Au(110)- $c(2 \times 2)$  LEED pattern. This re-generation could be repeated at least several times. Evidently, Sb diffuses readily into and out of the bulk, although the bulk concentration is limited to less than about 1%. We later exploited this tendency for the Sb to segregate to the surface by sputtering the sample while holding it at 700 K, allowing eventual depletion of Sb from the near-surface bulk region. Thus, the surfaces we measured undoubtedly contained some Sb in the bulk, but the concentration must be  $<1\%$  [9] and more likely as low as 0.01% [12] and provided no difficulties in the analysis.

XPS analysis [29] was performed using the Sb 3d and Au 4p<sub>3/2</sub> core levels, which have nearly the same binding energy (BE). Errors associated with uncertainties in the energy-dependent inelastic mean-free-path of the emitted photoelectrons are thereby minimized. Recommended values of the inelastic mean-free-path were obtained from Ref. [30], while photoelectric cross sections were derived from Ref. [31]. XP spectra from samples exhibiting a  $c(2 \times 2)$  surface reconstruction yielded a coverage of  $\theta_{\text{Sb}} = 0.5 \pm 0.1$  ML. The actual Sb coverage of the surface for which an extensive SXRD dataset was collected was not accurately determined, due to the lack of XPS in the SXRD endchamber. In later experiments, the intensity of the clean-surface  $(2 \times 1)$  and the Sb-induced  $c(2 \times 2)$  reconstruction peaks were monitored during Sb deposition. The  $(2 \times 1)$  peaks were extinguished before the appearance of the  $c(2 \times 2)$  peaks; evidently, these phases do not co-exist. The  $c(2 \times 2)$  peaks eventually reached a maximum at deposition time  $t_{\text{max}}$ , but made their initial appearance at  $\approx 0.6t_{\text{max}}$ . We can gain a rough understanding of the coverage range over which the  $c(2 \times 2)$  phase exists by assuming that the Sb was deposited at a constant rate and that the maximum  $c(2 \times 2)$  intensity corresponds to an ideal coverage of 0.5 ML. In this case, the weak  $c(2 \times 2)$  peaks first appeared at an Sb coverage of about 0.3 ML.

The surface was smooth and well-ordered, as judged by the CTR intensity and the reconstruction peak widths. The average correlation length of the domains [32] was better than 500 Å. The SRs show minimal modulation (with  $l$ ), indicating that the reconstructed region is confined to the outermost layer. In other words, there can be nearly no subsurface displacements, such as buckling, having the lateral length scale of the reconstruction.

## 5. In-plane fractional-order Patterson function

The self-convolution of some of the scattering data (Patterson function) can be computed directly to display strong interatomic scattering vectors (although without reference to any particular origin). A Patterson function  $P$  computed using fractional-order  $(hk)$  peaks only and  $l \approx 0$ :

$$P(x, y) = \frac{1}{N} \sum_{\{h,k\} \in \text{SR}, l \approx 0} |F_{hkl}|^2 \cos\{2\pi(hx + ky)\} \quad (1)$$

is particularly useful in identifying surface-related interatomic vectors. This function will not have false positive peaks above the noise level [33].

The fractional-order Patterson function for the present data plotted over a  $(2 \times 2)$  unit cell is shown in Fig. 3. There are strong peaks, located at  $2\mathbf{a}_1$ ,  $2\mathbf{a}_2$ ,  $(\mathbf{a}_1 + \mathbf{a}_2)$  and  $2(\mathbf{a}_1 + \mathbf{a}_2)$  [appearing at (2, 0), (0, 2), (1, 1) and (2, 2) in Fig. 3]. These peaks are merely the periodic repetition of the origin peak, reflecting the  $c(2 \times 2)$  symmetry of the diffraction pattern. (There are also several peaks in Fig. 3 that are an order of magnitude less intense; we believe these are simply the result of noise and the fact that data for precisely  $l = 0$  are not directly measurable.) As the surface has a coverage of  $\theta_{\text{Sb}} \approx 0.5$  ML, a structure where Sb occupies every other atop, long bridge, short bridge, or hollow site in a chess-board fashion is suggested. Note that the Patterson function alone cannot distinguish these possibilities.

We performed an initial calculation to compare these four models, and the results are summarized in Table 1. For purposes of this initial calculation, Sb atoms were held at the lateral  $(x, y)$  positions corresponding to the four high-symmetry sites under consideration (shown in Table 1), and Debye–Waller factors were held at the value corresponding to bulk Au at RT. The vertical ( $z$ ) positions of the Sb layer and the first Au layer were allowed to relax to minimize [34] the reduced  $\chi^2$ . Instead of citing the best-fitting

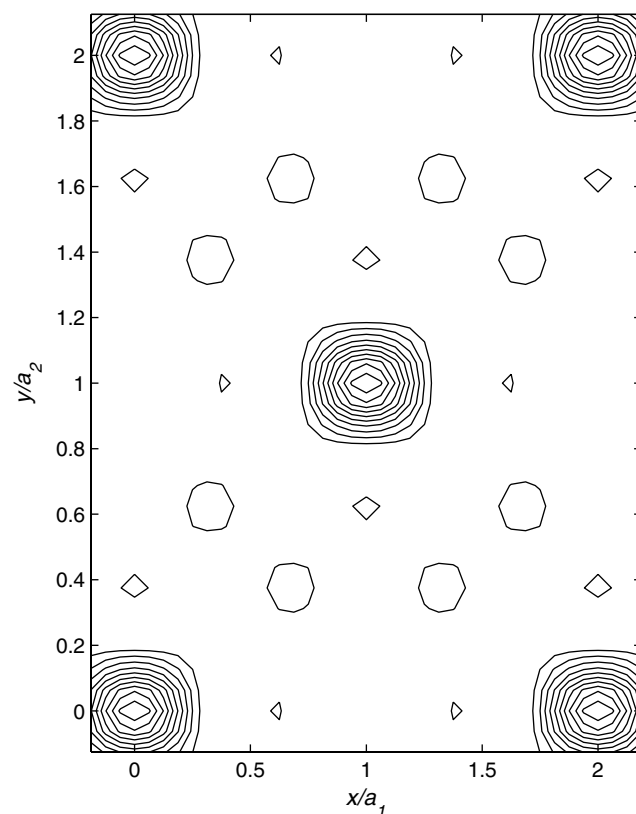


Fig. 3. Contour map of fractional Patterson function (self-convolution of the in-plane, fractional-order structure factors) showing strong interatomic scattering vectors in the  $(2 \times 2)$  unit cell. The only strong peak in the interior of the cell occurs at (1, 1).

Table 1  
Best-fit values of reduced  $\chi^2$  and resultant Sb–Au bondlength(s) for various high-symmetry models

	Sb <sub>1</sub> $\left(\frac{x}{a_1}, \frac{y}{a_2}\right)$	Sb <sub>2</sub> $\left(\frac{x}{a_1}, \frac{y}{a_2}\right)$	Sb–Au bondlength(s) (Å)	$\chi^2$
Atop	(0.5, 1.5)	(1.5, 0.5)	3.69	6.15
Short bridge	(0, 0.5)	(1, 1.5)	2.93	7.11
Long bridge	(0.5, 0)	(1.5, 1)	3.23	7.04
Hollow	(1, 0)	(0, 1)	2.62, 2.25	3.94
0.5 ML Sb	Sb: (1, 0)	Sb: (0, 1)	2.83	2.52
0.5 ML Au	Au: (0, 0)	Au: (1, 1)	2.76	

Lateral positions are normalized to the unit cell dimensions. The origin of the unit cell is at a surface substitutional site.

$z$ -positions in Table 1, we give an equivalent quantity, namely, the Sb–Au bondlength, to facilitate comparison between the different models. For comparison, the Au–Sb bondlength in AuSb<sub>2</sub> is 2.763 Å [35]. In agreement with our chemical intuition, occupation of hollow sites is clearly preferred. However, attempts to further refine this structure by relaxing other fitting parameters never resulted in a satisfactory fit, and the best-fit model included unphysical values of some of the fitting parameters. Thus, we seek a better model of the surface geometry.

A further conventional approach to extract information from the scattering data, termed difference Fourier synthesis, is useful when most of the structural elements of the reconstruction have already been identified [36]. Essentially, this method makes the approximation that the (unknown) phase of the surface structure factors  $F_{hk}$  are nearly the same as the (calculable) phases of the scattering arising from the elements of the reconstruction known so far. This approximation allows one to directly synthesize the difference between the true structure and the tentative model. In our case, the results from this exercise were ambiguous, with no clear, physically reasonable peaks in the distribution. This could be because the approximation upon which the method relies was not sufficiently fulfilled when (as we shall see) only half of the atoms in the reconstruction had been identified. Another possible complication comes from the need to place the measured structure factors on an absolute scale to use this approach.

Before presenting the results of our direct method, we first consider why all desired information is not present in the conventional partial Patterson function. If one understands the in-plane fractional-order Patterson function above to reveal all interatomic vectors of the projected surface structure, the calculated Patterson function is consistent only with a model of a single atom per  $c(2 \times 2)$  surface unit cell. However, as we point out below, in the case of any  $c(2 \times 2)$  overlayer such a partial Patterson function (1) cannot produce positive peaks corresponding to interatomic vectors equal to bulk lattice vectors *even if such vectors do exist in the true surface structure*. The proof of this statement follows.

For fractional-order reflections, the in-plane Laue indices are

$$(h, k) = \left(m + \frac{1}{2}, n + \frac{1}{2}\right), \quad (2)$$

where  $m$  and  $n$  are integers. Thus the cosine term in (1) takes the form

$$\cos \left\{ 2\pi \left[ \left(m + \frac{1}{2}\right)x + \left(n + \frac{1}{2}\right)y \right] \right\}, \quad (3)$$

which for integer  $x$  and  $y$  (corresponding to bulk lattice vectors) reduces to  $\cos[\pi(x+y)]$  and is positive only if  $x+y$  is a multiple of two, e.g.  $(x, y) = (0, 0), (0, 2), (1, 1), (2, 0),$  or  $(2, 2),$  etc. These are the lattice vectors of a  $c(2 \times 2)$  surface unit cell and correspond to origin peaks on the Patterson map, which are the only ones observed in Fig. 3. Thus, at least in the case where interatomic vectors in the adlayer are equal to 2D bulk lattice vectors, it is dangerous to rely only on the positive peaks of the fractional Patterson function.

## 6. Results from direct method

However, as we demonstrate below, since it uses all the measured data (from CTRs as well as SRs) our direct method does not suffer from this limitation, and does in fact reveal four atoms per  $c(2 \times 2)$  surface unit cell, with dissimilar atoms separated by bulk in-plane lattice vectors. Furthermore, it reveals directly a picture of the entire 3D structure of the surface unit cell. The output of this algorithm applied to the measured data set is shown in Fig. 4. The recovered electron density in the near-surface region indicates hollow sites are indeed occupied. However, significant electron density is recovered in *every* hollow site, not every other one, but the charge density in half the sites is greater than in the other half. Thus, we identify a model where every other hollow site is occupied by Au adatoms, while the remaining half is occupied by Sb adatoms. Fig. 5 depicts a schematic of the proposed arrangement. Note that such a model is consistent with the fractional Patterson function in Fig. 3, as the additional interatomic vectors introduced between the Au and Sb surface sublattices, such as  $\mathbf{a}_1$  [i.e., (1, 0)] and  $\mathbf{a}_2$  [i.e., (0, 1)], coincide with substrate lattice vectors and would not appear in the fractional Patterson function as discussed above. Thus, the fractional Patterson function cannot distinguish between any of the simple models having only 0.5 ML surface Sb, and the one with an additional 0.5 ML Au. Preliminary conventional fitting of the latter model, subject to the same restrictions on free parameters as used for the other models, yields a reduced  $\chi^2$  of 2.52, significantly better than the other models. Since not just the adsorption site, but also the number and identity of the species in the surface unit cell is different for these models, it is obvious that conventional refinement from one of the original starting points suggested by the fractional Patterson function would never be able to converge to this arrangement.

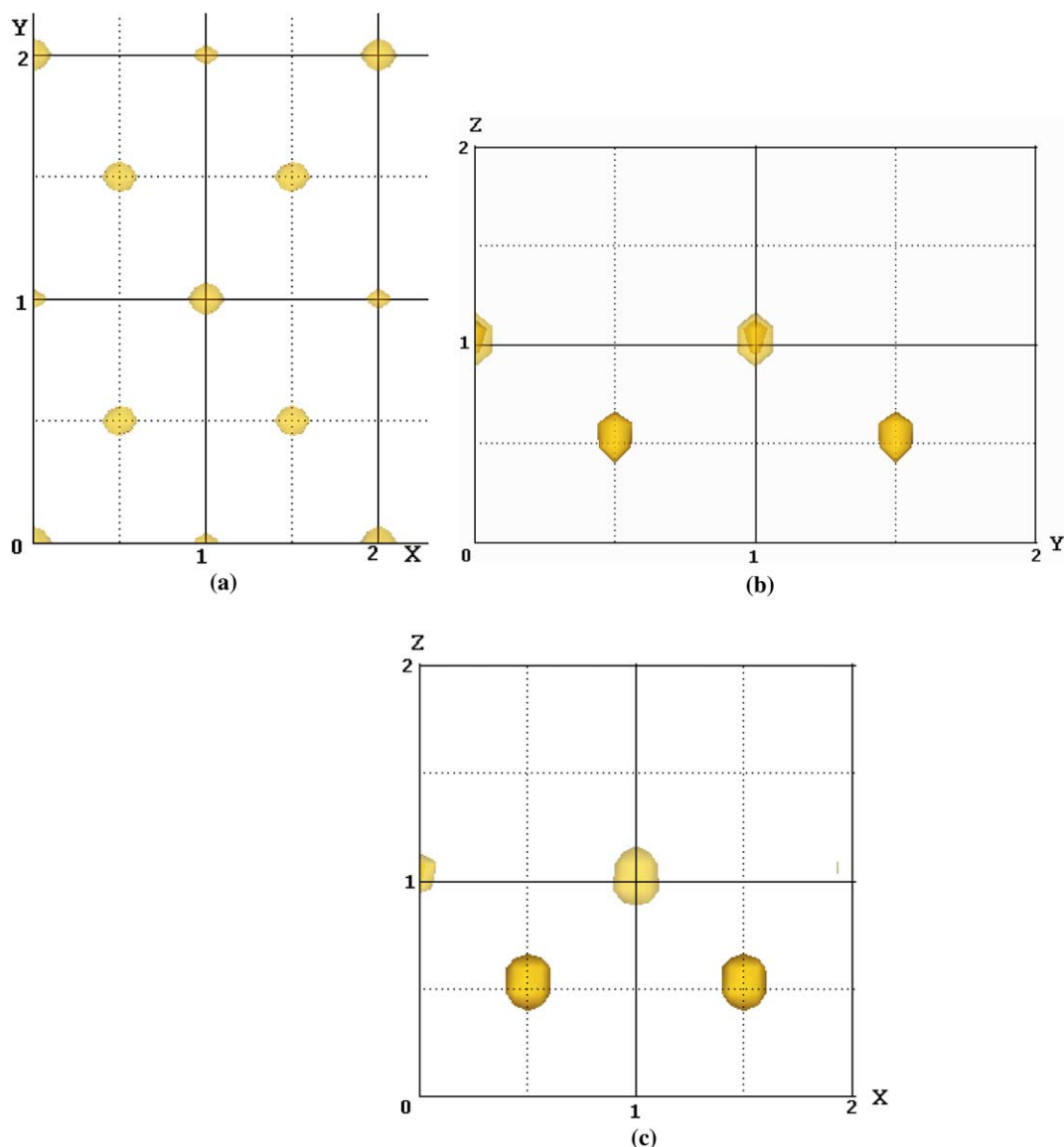


Fig. 4. Electron density in near-surface region recovered by direct-method algorithm. (a)–(c) Orthographic projection through the (a)  $xy$ , (b)  $yz$ , and (c)  $xz$  planes. Isosurfaces of electron density are shown. (d) and (e) Two-dimensional cuts through recovered electron density at  $xy$  planes located at (d)  $z/a_3 = 1.125$ , and (e)  $z/a_3 = 0.625$ , corresponding to the plane of surface atoms and second-layer substrate atoms, respectively. Warm colors represent high-electron density, while cool colors represent lower electron density.

## 7. Structure refinement

Next, additional free parameters are relaxed in order to optimize the fit. In addition to the  $z$  positions of the Sb and surface and second-layer Au atoms, the Debye–Waller parameters  $B$  (assumed isotropic) of each layer were allowed to vary.<sup>1</sup> With these parameters free, the reduced  $\chi^2$  reached a value of 1.45 with the values shown in the left-hand side of Table 2. Thus, the evidence for correctness of the 0.5 ML Sb/0.5 ML Au substitutional model is quite strong.

<sup>1</sup> The Debye–Waller parameter  $B$  is related to the Debye–Waller factor  $\exp(-2M)$  through  $M = B \sin^2 \theta / \lambda^2$ .

No statistically significant reduction in reduced  $\chi^2$  was obtained upon allowing any of the atoms to shift laterally from the high-symmetry hollow sites. Note that, due to the large value of parallel momentum transfer  $q_{\parallel}$  accessible with SXRD in general [37] and used in this study in particular ( $q_{\parallel, \text{Max}} \approx 10 \text{ \AA}^{-1}$ ), we are very sensitive to such displacements. Further note that we thoroughly investigated models where the four possible symmetry-related domains allowed by the  $pmm$  substrate were present, but still found no evidence for spontaneous displacement away from the hollow sites. Also, allowing increased surface roughness, allowing anisotropic Debye–Waller factors, allowing relaxation in the third or deeper layers, or allowing buckling consistent with the  $c(2 \times 2)$  symmetry in the second, third or deeper layers (see Section 9), all failed to improve the fit.

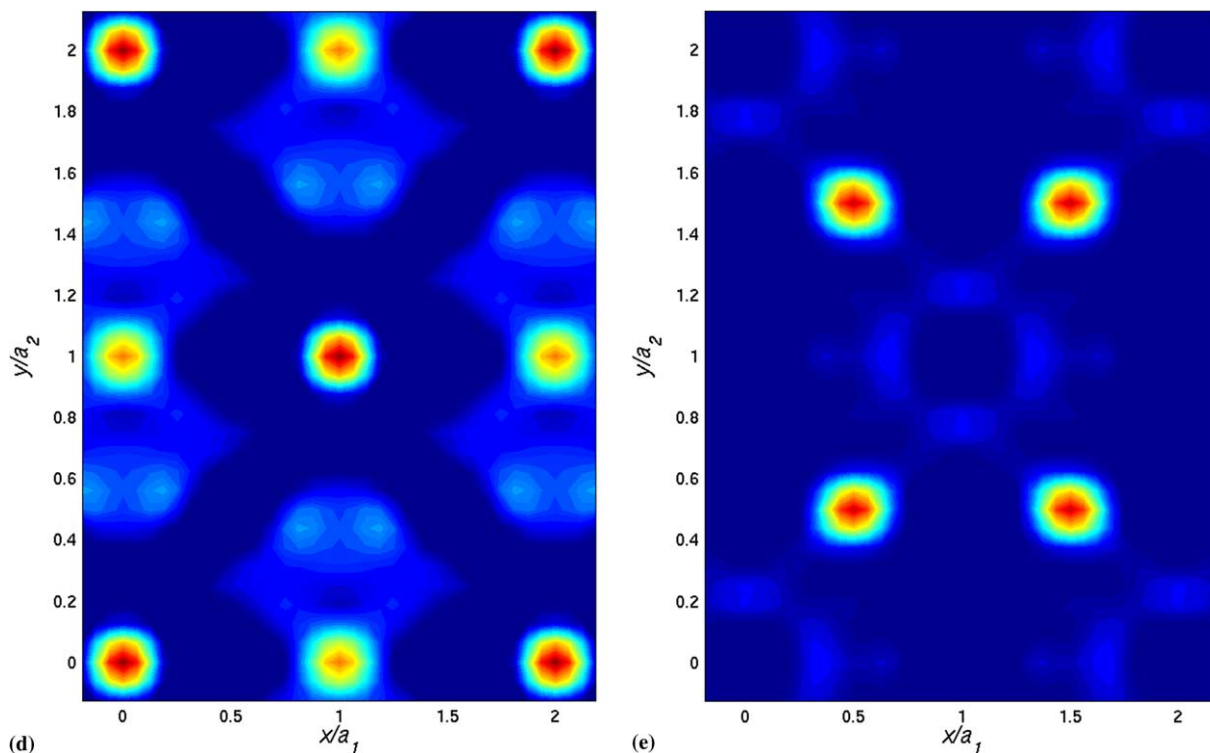


Fig. 4 (continued)

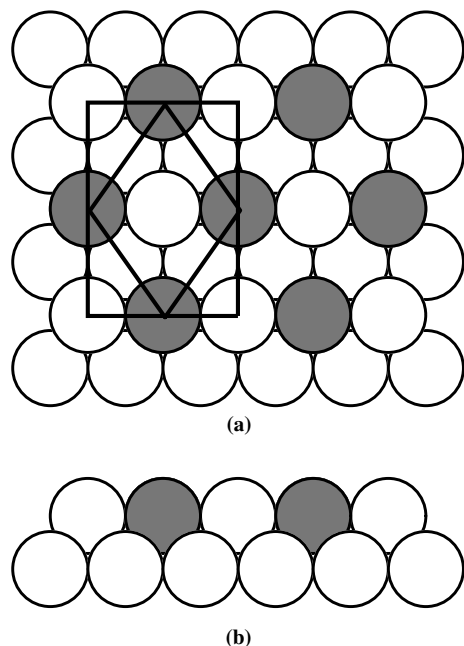


Fig. 5. Hard-sphere model of Sb/Au(110)- $c(2 \times 2)$  structure. Au atoms are open, Sb atoms are filled. (a) Plan view. Primitive and  $c(2 \times 2)$  unit cells are indicated. (b) Side view along  $[001]$  direction.

Although the fit obtained with the parameters in the left-hand side of Table 2 is good, one characteristic appears questionable. The best-fit values of the Debye–Waller parameters  $B$  for the surface Au and Sb atoms are some-

Table 2

Best-fit structural parameters for Sb/Au(110), with and without variable occupancy of Au and Sb sites

	Fixed occupancy	Variable occupancy
$d_{\text{Sb-Au1}}$ ( $\text{\AA}$ ) (rumple)	$-0.17 \pm 0.04$	$-0.21 \pm 0.04$
$\Delta d_{\text{Au1-2}}$ ( $\text{\AA}$ )	$-0.15 \pm 0.03$	$-0.12 \pm 0.03$
$\Delta d_{2-3}$ ( $\text{\AA}$ )	$0.15 \pm 0.03$	$0.13 \pm 0.03$
$B_{\text{Sb}}$ ( $\text{\AA}^2$ )	$2.8 \pm 0.2$	$1.3 \pm 0.2$
$B_{\text{Au1}}$ ( $\text{\AA}^2$ )	$3.5 \pm 0.2$	$1.5 \pm 0.2$
$B_{\text{Au2}}$ ( $\text{\AA}^2$ )	$1.1 \pm 0.2$	$1.5 \pm 0.2$
Sb occupancy	N/A	$0.78 \pm 0.05$
Au <sub>1</sub> occupancy	N/A	$0.71 \pm 0.05$
Reduced $\chi^2$	1.45	0.90

what high. For example, the value  $B = 3.5 \text{ \AA}^2$  corresponds to a root-mean-square vibrational amplitude  $\langle u^2 \rangle^{1/2}$  of  $0.21 \text{ \AA}$ . However, the Debye–Waller  $B$  parameters may describe static, as well as dynamic, displacements from the nominal position. Thus, the enhanced values of  $B$  may be related to an imperfectly ordered surface phase, rather than a dynamic vibrational amplitude. (Note that the Debye–Waller factor should not be affected by small domain sizes, which would cause broadening of the surface peaks, but should not affect their intensity. Moreover, recall that the average domain size for this surface was found to be in excess of  $500 \text{ \AA}$ .) Rather, we need to consider disorder within a domain. Since the  $c(2 \times 2)$  reconstruction persists over a range of Sb coverages, there may be incomplete occupation of the surface atomic sites. Upon introducing a free param-

eter allowing for partial occupancies by surface Au and Sb, a significant reduction in the reduced  $\chi^2$  to 0.90 was found for occupancies of  $\approx 0.7$ – $0.8$ . At the same time, the Debye–Waller parameters for the Sb and top-layer Au dropped to  $B \approx 1.5 \text{ \AA}^2$ ; these correspond to more reasonable values of the vibrational amplitude of  $\langle u^2 \rangle^{1/2} \approx 0.14 \text{ \AA}$ . The central values of the positional parameters did change slightly from the fully occupied model, but by amounts less than the cited uncertainty (see Table 2). The Sb coverage implied by the partial-occupancy fit parameter is just within range of XPS-determined coverages for surfaces that display the  $c(2 \times 2)$  reconstruction observed by LEED in the UHV chamber at the University of Wisconsin-Milwaukee, and is well within the range inferred from later SXRD measurements of the intensity of a  $c(2 \times 2)$  peak with continuing Sb deposition. (Note that the uncertainties in the occupancies in Table 2 are uncertainties in the fitting parameters only, not in the Sb coverage measurement.) Moreover, the SXRD endstation at the NSLS lacks XPS capabilities, so an accurate coverage measurement for the SXRD-measured surface is not available, i.e., the measured surface could have been prepared with an Sb coverage that was slightly too low. Thus, the structural parameters listed in the right-hand side of Table 2, derived assuming partial occupancy of the surface sites, are preferred. Recall that the clean-surface  $(2 \times 1)$  peaks were extinguished before the appearance of the  $c(2 \times 2)$  peaks, so no co-existence of these phases occurred.

## 8. Thermal stability

Having established the surface structure, we proceeded to probe the thermal stability of this surface arrangement. Accordingly, we examined a reflection that corresponds to the surface reconstruction, viz., the  $(\frac{1}{2} \frac{1}{2} 0.39)$ , while heating the sample. We found that the reconstruction persisted to surprisingly high temperatures. Fig. 6(a) displays the square root of the peak intensity, which is proportional to the structure factor  $F$ , of this reflection as a function of the substrate temperature  $T$ . It is evident that the structure factor initially increases upon heating up to about 600 K, before falling dramatically as the substrate temperature exceeded 800 K. Nevertheless, there is still significant intensity at 900 K. For comparison, the bulk melting point of  $\text{AuSb}_2$  is 732 K [8]. The process was reversible upon cooling; the peak re-emerged just above 900 K, and grew in intensity upon cooling, recovering essentially all of its intensity by 780 K.

Fig. 6(b) shows the reflected intensity as a function of scanning the sample about its surface normal (i.e., an  $\omega$ -scan) for several substrate temperatures (indicated by vertical lines in Fig. 6(a)). The  $\omega$ -scans were well fit by a Lorentzian function (solid lines in Fig. 6(b)), providing quantitative estimates of the peak widths. The peak broadened only slightly as the sample temperature increased. Up to  $\sim 700$  K, the peak FWHM was  $0.195^\circ$ , and it increased somewhat, to  $0.22^\circ$ , at 895 K; these values correspond

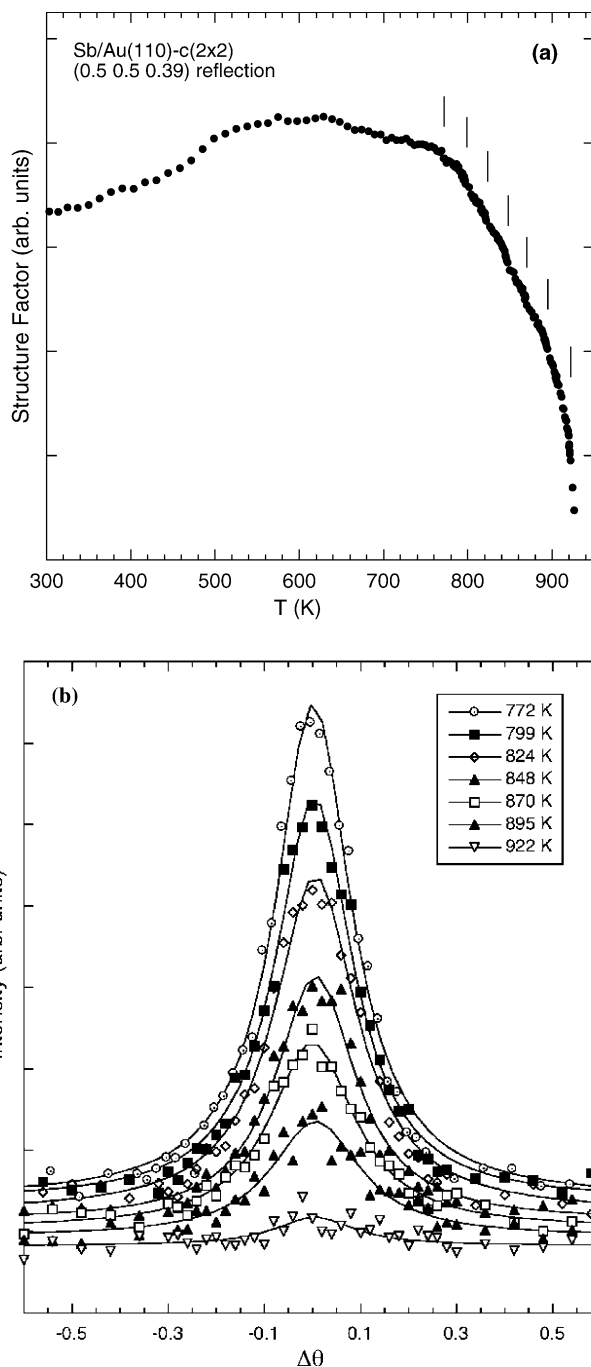


Fig. 6. (a) Square root of the peak intensity of the  $(\frac{1}{2} \frac{1}{2} 0.39)$  reflection as a function of temperature. The temperatures at which the  $\omega$ -scans displayed in (b) were acquired are indicated by the vertical lines. (b) Reflected intensity as a function of sample rotation angle (i.e.,  $\omega$ -scans) acquired at several substrate temperatures.

[32] to correlation lengths (i.e., domain sizes) of  $430 \text{ \AA}$  at 700 K, falling to  $380 \text{ \AA}$  at 895 K.

## 9. Discussion

First, we consider the size of the dataset required for the direct method we demonstrate here, and compare this to the size typically acquired for conventional analysis. Of

course, both approaches build up a knowledge of modulations in the electron density in reciprocal space by measuring structure factors  $\{F(\vec{q})\}$ . Thus, for both techniques, the experimenter desires to acquire as many structure factors as time allows. Traditionally, SXRD experiments focused most attention on the in-plane ( $l \approx 0$ ) structure factors, and supplemented this information with a few out-of-plane (CTR or SR) measurements to help determine the registry of the surface unit cell [36], so data sets were often reasonably small. However, as new instruments with additional degrees of freedom made out-of-plane measurements more routine and reliable [28], and as greater brilliance from improved synchrotron sources greatly reduced measurement times, later investigators began to rely more heavily on out-of-plane measurements for high-quality structural determinations [38].

The dataset employed here (558 independent reflections) is significantly larger than used in many earlier studies of comparable unit cell size. We have found, as expected [39], that numerical stability of our algorithm increases with frequency of reciprocal-space sampling. We estimate that we have employed four times more data than comparable published works employing only conventional analysis. However, we argue that the tradeoff between data collection time and ability to generate a starting model is not a significant disadvantage, and becomes a significant advantage for larger surface unit cells.

While it is, of course, desirable to minimize time required to acquire data, the time required to analyze data should also be taken into account. The data presented here were acquired over  $\sim 5$  days of measuring time (after the sample was prepared and aligned) at a bending magnet beamline of a second-generation synchrotron source. In similar experiments we have conducted at a third-generation synchrotron, those measurements would have taken approximately one day of measuring time. On the other hand, trying to refine many possible initial structural models can consume many days of analysis time, with no guarantee the correct model will be identified.

This factor becomes more important for more complicated reconstructions. For the following calculation, we assume that a surface unit cell of dimensions  $S \times T$  times larger than the bulk unit cell will contain approximately  $nST$  atoms, where  $n$  is the number of atoms in the bulk unit cell. The dataset required for our method should be correspondingly  $ST$  times larger, and the total number of free parameters is of the order of  $3nST$ . A systematic search, wherein each parameter describing a model structure is evaluated at, say,  $p$  different values, quickly becomes intractable as  $p^{3nST}$  calculations must be performed [40]. Instead, the experimenter must envision the subset of these structural models that are likely to be correct, and then try to refine those models by comparison to the data. This process may easily become the limiting factor in solving the structure. The primary purpose of the direct method used here is to relieve the experimenter of that necessity by providing a small number of initial estimates of

atomic positions that can then be refined by conventional means.

Next, we briefly discuss the major structural findings, summarized in Table 2 and Fig. 5. The change in the spacing of the first and second Au layers,  $\Delta d_{\text{Au1-2}}$ , reveals a contraction of 0.12 Å, which is about 9% of the interlayer spacing. Meanwhile, the change in the second-to-third layer spacing,  $\Delta d_{2-3}$ , shows an expansion of 0.13 Å, or about 9%. This oscillatory relaxation behavior is completely consistent with that observed on a host of metallic surface systems [41].

The Sb atoms are sevenfold coordinated, and are displaced inward from the surface Au atoms ( $d_{\text{Sb-Au1}}$  in Table 2) by about 0.2 Å. To help understand this rumpling, we consider the resultant bond lengths to the nearby Au atoms. The Sb forms one bond of 2.68 Å to the Au atom in the third layer directly below, four bonds of 2.73 Å to the second-layer Au atoms, and two bonds of 2.89 Å to the Au atoms in the same (first) layer. This provides a weighted average Au–Sb bond length of 2.77 Å. For comparison, the Sb–Au bond length in bulk AuSb<sub>2</sub> is 2.763 Å [35]. Rumpling upon alloy formation depends on the metallic radius of the adsorbed element: an adsorbate that is larger than the host atoms will tend to be displaced outwards from the surface [42]. However, it has been demonstrated that the effect is generally smaller than a simple hard-sphere picture would imply, and this reduction has been attributed to the tensile stress present at a solid surface due to the undercoordination of the surface atoms; in fact, relief of that stress is thought to drive alloy formation [42]. To apply this picture, one needs to identify the correct metallic radius for the adsorbate. In the present case, this can be somewhat confusing, as the bulk bonding of the metalloid Sb is quite different than that of metallic Au, and there is not even universal agreement as to which of these should have the larger radius [43]. It has been argued, however, that the bond length found in a bulk alloy of the elements in question is most relevant [42]. A center-to-center separation of 2.763 Å (as in AuSb<sub>2</sub>) between first-layer Sb and second-layer Au, taken as hard spheres, would result in a vertical displacement of 1.18 Å, compared to the measured value  $d_{220} + \Delta d_{\text{Au1-2}} + d_{\text{Sb-Au1}}$  of 1.11 Å. Given the tendency for small inward displacements that serve to relieve tensile surface stress, our finding is consistent with the established picture.

As mentioned above, there was no statistically significant improvement in the fit upon allowing buckling in the second or third layers (that is, allowing the  $z$ -positions of the two distinct Au atoms in the second or third Au layers to vary individually). However, there was a slight improvement of about 0.05 in the reduced  $\chi^2$  if we allowed third-layer buckling. Note that such a movement is allowed by the  $c(2 \times 2)$  symmetry, and it would be reasonable to expect that the Au atoms, which are in different chemical environments, would occupy slightly different sites. However, nearly equally good fits were arrived at with either of the two distinct Au atoms being located higher,

indicating that any such buckling is too small to observe reliably.

It appears that the detailed structural parameters may depend on the temperature. In Fig. 6(a), an initial increase in intensity of a peak indicative of the  $c(2 \times 2)$  phase was observed as the sample was heated to about 600 K. The data in Fig. 6 were acquired while the sample was being re-heated after initial preparation. Thus, this increase might simply be attributed to improved long-range order. However, the width of the peak in the  $\omega$ -scans did not change from RT, ruling out that supposition. Another possible explanation is that the surface was initially deficient in Sb, and the re-annealing allowed more Sb to diffuse from the bulk to the surface. This is unlikely because the surface was initially prepared by Sb deposition, so no mechanism for a Sb-rich bulk and Sb-deficient surface is evident. Moreover, and most tellingly, the same trend, where the peak intensity was greater at intermediate temperatures than at RT, was observed upon cooling as well. Thus, the most likely scenario is that thermal agitation alters the precise structural parameters in a way that increases the surface structure factor for a  $c(2 \times 2)$  unit cell. We have no information on what such a distortion would be, as we did not collect any other reflections at elevated temperatures.

One of the more surprising results of our study was the thermal stability exhibited, where the  $c(2 \times 2)$  phase persisted to above 900 K. On the clean surface, the well-known  $(2 \times 1)$  phase undergoes a deconstruction to a disordered  $(1 \times 1)$  phase at 735 K [24,25], and the surface roughens at 784 K [24]. In the Sb–Au bulk system, the Sb eutectic temperature, reached at 35.5 at.% Sb, is about 630 K, and bulk  $\text{AuSb}_2$  melts at 732 K [7,8]. Thus, a much lower temperature for the removal of this surface phase would reasonably be expected. Its robustness is presumably related to the Sb–Au chemical affinity and the lack of bulk solid solubility.

From our studies, we cannot conclude what the origin of the eventual deconstruction at  $>900$  K is. There are at least two possibilities. In one scenario, the Sb could diffuse into the bulk or evaporate at elevated temperatures, leaving behind a mostly Au surface layer, which would not be reconstructed at that temperature. Another possibility is that the surface Sb and Au atoms undergo an order–disorder transition; the Sb would still be confined to the surface and located in hollow sites in this scenario, but the long-range chessboard ordering of Sb and Au atoms would disappear due to thermally induced exchange of Sb and Au atoms between the two possible surface sublattices. In such an order–disorder transition, intensity would be transferred from the sharp Bragg component into a broad diffuse peak as the critical temperature  $T_c$  is approached [44]. There is little evidence for this transfer in the scans shown in Fig. 6(b), but wider scans are required to ascertain the lineshape in the vicinity of  $T_c$  definitively. Thus, based on available data, we are not able to make a conclusion as to what mechanism led to the deconstruction. The neces-

sary measurements will be undertaken in future experiments.

As previously mentioned, there have been no prior reports of Sb adsorption on the Au(110) surface. However, previous studies of surface structures formed by Sb on Au(100) [12] and Au(111) [45,46] surfaces have been interpreted as arising from a low-index plane of the  $\text{AuSb}_2$  bulk compound. The Au(100) study observed a complicated two-domain  $(4 \times 22)$  LEED pattern, which was attributed to the superposition of a  $\text{AuSb}_2(111)$  double layer on a relatively unperturbed Au(100) substrate [12]. The two Sb/Au(111) studies reached dissimilar conclusions from each other. The earlier work reported a  $(2\sqrt{3} \times 2\sqrt{3})R30^\circ$  LEED pattern, which was attributed to a single  $\text{AuSb}_2(111)$  plane formed from Sb atoms occupying substitutional sites on the Au(111) surface [45]. Thus, these two studies point out the possibility that  $\text{AuSb}_2(111)$  planes may form particularly stable structures. However, the later Sb/Au(111) work [46] reached a somewhat different conclusion based on atomic-resolution scanning tunneling microscopy (STM) images. The square symmetry and topographical features observed were attributed to formation of  $\text{AuSb}_2(100)$  layers on top of the Au(111) substrate [46]. Despite any discrepancies among these surfaces, it is clear that intermetallic alloy formation has previously been demonstrated in the Sb/Au surface system. It remains unclear whether simple substitution into the Au positions, as we have measured here and is reported (if not so interpreted) by Ref. [45] is the norm, or if the driving force for the formation of  $\text{AuSb}_2$  planes is so strong as to favor independent planes of the bulk compound (as reported in Refs. [12,46]) under many conditions.

The (110) face of a fcc crystal is the most open of its low-index surfaces. Most likely as a result, (110) surfaces of some materials are reconstructed in their clean state, while others can be induced to form related reconstructions upon adsorption of foreign species. Therefore, it is also relevant to consider systems related to the one reported here, such as the adsorption of different elements onto the Au(110) surface or the adsorption of Sb onto (110) surfaces of other fcc crystals.

Adsorption of 0.5 ML K onto a heated Au(110) surface results in the formation of a  $c(2 \times 2)$  reconstruction. A medium energy ion scattering (MEIS) study concluded that K atoms are located in substitutional sites in a chessboard fashion, [47], i.e., the same structure as concluded here. However, the large difference in atomic radii of K and Au, and in particular the astonishing change in the effective atomic radius of K upon formation of compounds with Au [48], makes further comparisons difficult. Note that in the MEIS study, the K atoms were found to lie 1.05 Å above the Au atoms in the surface plane, compared to a much smaller displacement of opposite sign (−0.21 Å) of Sb atoms here. Another interesting finding was that there was a pronounced buckling (of 8%) in the third layer, with the Au atoms directly below the K adatom being displaced towards the surface and those beneath the top-layer Au

atoms being pushed into the bulk. Although we should be sensitive to such a buckling due to the large value of perpendicular momentum transfer  $q_{\perp}$  used, we find no reliable evidence of this buckling for the Sb/Au(110)-c(2×2) system as described above.

Perhaps a more closely related system is that of Sb/Ag(110)-c(2×2), which was reported for the first time very recently [43]. This LEED-I/V study found the same basic structure as that reported here upon adsorption of 0.5 ML Sb, namely, the Sb occupies every other surface substitutional site, and 0.5 ML Ag completes the first layer. Results of their structural analysis are very similar to those reported here: they find a first-layer contraction, a second-layer expansion, and they also find Sb displaced slightly inwards compared to the outermost Ag atoms. They report no evidence for a second- or third-layer buckling, although it is unclear if they considered such a distortion. However, the overall magnitude of their reported relaxations was uniformly smaller than in the Au case. They reported a first-layer contraction  $\Delta d_{\text{Ag}1-2}$  of about -5%, and a second-layer expansion  $\Delta d_{23}$  of about +2.5%, and an inward Sb displacement of about -4%, compared to our corresponding values of -9%, +9%, and -15%.

## 10. Conclusions

We have determined the structure of a new surface phase, Sb/Au(110)-c(2×2) using LEED, XPS, and SXRD. A new direct-method algorithm [14–17] was used to directly, and independently of any model, recover the charge density in the near-surface region. This recovery suggested a model of a surface phase that could be subsequently refined by conventional fitting to be in excellent quantitative agreement with the scattering data. We conclude that the surface is formed by 0.5 ML Sb and 0.5 ML Au, arranged as a c(2×2) substitutional alloy. This phase demonstrates remarkable thermal stability, enduring up to annealing temperatures of 900 K, which is far above the expected stability limit of the reconstruction.

## Acknowledgement

Discussions with A.P. Baddorf, K. Evans-Lutterodt, J.P. Hill, I.K. Robinson, W. Moritz, and H. Zajonz are deeply appreciated. The use of the X22C beamline is gratefully acknowledged. This material is supported by the US DOE under Award No. FG02-OIER45926 and by the NSF under Grant Nos. DMR-9815092 (D.K.S.) and DMR-9984442 (P.F.L.). P.F.L. acknowledges support from the Research Corporation. Work at BNL is supported by US DOE under Contract No. DE-AC02-98CH10886.

## References

- [1] Y.M. Swe, I. Lee, T. Htay, M. Aung, *Resource Geol.* 54 (2004) 197.
- [2] A.G. Chynoweth, W.L. Feldmann, C.A. Lee, R.A. Logan, G.L. Pearson, P. Aigrain, *Phys. Rev.* 118 (1960) 425.

- [3] J.H. Kim, S.W. Jeong, H.M. Lee, *J. Electron. Mater.* 31 (2002) 557.
- [4] H. Yasuda, H. Mori, *Z. Phys. D* 40 (1997) 140.
- [5] D. Besson, M. Treilleux, A. Hoareau, L. Bardotti, B. Prevel, A. Perez, C. Esnouf, *Eur. Phys. J. D* 9 (1999) 513.
- [6] H.-G. Boyen, A. Cossy-Favre, P. Oelhafen, A. Siber, P. Ziemann, C. Lauinger, T. Moser, P. Häussler, F. Baumann, *Phys. Rev. B* 51 (1995) 1791.
- [7] W.G. Moffatt, *The Handbook of Binary Phase Diagrams*, Genium, Schenectady, 1986.
- [8] M. Hansen, *Constitution of Binary Alloys*, McGraw-Hill, New York, 1958.
- [9] P.-Y. Chevalier, *Thermochim. Acta* 155 (1989) 211.
- [10] J.R. Chelikowsky, *Surf. Sci.* 139 (1984) L197.
- [11] A. Christensen, A.V. Ruban, P. Stoltze, K.W. Jacobsen, H.L. Skriver, J.K. Nørskov, F. Besenbacher, *Phys. Rev. B* 56 (1997) 5822.
- [12] G.K. Wertheim, J.E. Rowe, D.N.E. Buchanan, H.L. Polite, H. Shigeekawa, *Phys. Rev. B* 38 (1988) 9606.
- [13] L.D. Marks, *Phys. Rev. B* 60 (1999) 2771.
- [14] D.K. Saldin, R.J. Harder, V.L. Shneerson, W. Moritz, *J. Phys. Condens. Matter* 13 (2001) 10689.
- [15] D.K. Saldin, R.J. Harder, H. Vogler, W. Moritz, I.K. Robinson, *Comput. Phys. Commun.* 137 (2001) 12.
- [16] D.K. Saldin, R.J. Harder, V.L. Shneerson, W. Moritz, *J. Phys. Condens. Matter* 14 (2002) 4087.
- [17] P.F. Lyman, V.L. Shneerson, R. Fung, R.J. Harder, E.D. Lu, S.S. Parihar, D.K. Saldin, *Phys. Rev. B* 71 (2005) 081402(R).
- [18] S.R. Andrews, R.A. Cowley, *J. Phys. C* 18 (1985) 6427.
- [19] I.K. Robinson, *Phys. Rev. B* 33 (1986) 3830.
- [20] J.R. Fienup, *Opt. Lett.* 3 (1978) 27.
- [21] R. Fung, V.L. Shneerson, D.K. Saldin, S.S. Parihar, H.T. Johnson-Steigelman, P.F. Lyman, unpublished.
- [22] D. Gibbs, B.M. Ocko, D.M. Zehner, S.G.J. Mochrie, *Phys. Rev. B* 42 (1990) 7330.
- [23] W. Moritz, D. Wolf, *Surf. Sci.* 88 (1979) L29; W. Moritz, D. Wolf, *Surf. Sci.* 163 (1985) L655.
- [24] D.T. Keane, P.A. Bancel, J.L. Jordan-Sweet, G.A. Held, A. Mak, R.J. Birgeneau, *Surf. Sci.* 250 (1991) 8.
- [25] J. Sprösser, B. Salanon, J. Lapujoulade, *Europhys. Lett.* 16 (1991) 283.
- [26] L. Ley, S. Kowalczyk, R. Pollak, D.A. Shirley, *Phys. Rev. Lett.* 29 (1972) 1088.
- [27] S. Doniach, M. Sunjic, *J. Phys. C* 3 (1970) 285.
- [28] E. Vlieg, *J. Appl. Cryst.* 30 (1997) 532.
- [29] M.P. Seah, in: D. Briggs, M.P. Seah (Eds.), *Practical Surface Analysis by Auger and X-ray Photoelectron Spectroscopy*, John Wiley & Sons, 1983.
- [30] C.J. Powell, A. Jablonski, *NIST Electron Inelastic-Mean-Free-Path Database—Version 1.1*, National Institute of Standards and Technology, Gaithersburg, MD, 2000.
- [31] D.T. Cromer, D. Liberman, *J. Chem. Phys.* 53 (1970) 1891.
- [32] E. Vlieg, J.F. van der Veen, S.J. Gurman, C. Norris, J.E. MacDonald, *Surf. Sci.* 210 (1989) 301.
- [33] J. Bohr, R. Feidenhans'l, M. Nielsen, M. Toney, R.L. Johnson, I.K. Robinson, *Phys. Rev. Lett.* 56 (1986) 2878.
- [34] E. Vlieg, *J. Appl. Cryst.* 33 (2000) 401.
- [35] S. Furuseth, K. Selte, A. Kjekshus, *Acta Chem. Scand.* 19 (1965) 735.
- [36] I.K. Robinson, D.J. Tweet, *Rep. Prog. Phys.* 55 (1992) 599.
- [37] E. Vlieg, I.K. Robinson, K. Kern, *Surf. Sci.* 233 (1990) 248.
- [38] S. Ferrer, X. Torrelles, V.H. Etgens, H.A. van der Vegt, P. Fajardo, *Phys. Rev. Lett.* 75 (1995) 1771.
- [39] J. Miao, D. Sayre, H.N. Chapman, *J. Opt. Soc. Am. A* 15 (1998) 1662.
- [40] J.B. Pendry, K. Heinz, W. Oed, *Phys. Rev. Lett.* 61 (1988) 2953.
- [41] See, e.g., A.M. Rodriguez, G. Bozzolo, J. Ferrante, *Surf. Sci.* 289 (1993) 100.
- [42] D.P. Woodruff, E. Vlieg, in: D.P. Woodruff (Ed.), *Surface Alloys and Alloy Surfaces, The Chemical Physics of Solid Surfaces*, vol. 10, Elsevier, 2002, p. 277.

- [43] V.B. Nascimento, R. Paniago, A. de Siervo, C.M.C. de Castilho, R. Landers, E.A. Soares, V.E. de Carvalho, *Surf. Sci.* 572 (2004) 337.
- [44] M.E. Fisher, R.J. Burford, *Phys. Rev.* 156 (1967) 583.
- [45] P. Ma, A.J. Slavin, *J. Vac. Sci. Technol. A* 11 (1993) 2003.
- [46] B. Stegemann, T.M. Bernhardt, B. Kaiser, K. Rademann, *Surf. Sci.* 511 (2002) 153.
- [47] P. Häberle, T. Gustafsson, *Phys. Rev. B* 40 (1989) 8218.
- [48] R.E. Watson, M. Weinert, *Phys. Rev. B* 49 (1994) 7148.